RSC Advances

ROYAL SOCIETY OF CHEMISTRY

PAPER

View Article Online
View Journal | View Issue

Check for updates

Cite this: *RSC Adv.*, 2025, **15**, 25372

Doped photocatalyst immobilization on tubular surface: continuous photocatalysis of pharma drugs under visible light†

Rahul Binjhade,[a] Raka Mondal[b] and Sourav Mondal *[a]

This study presents the fabrication and characterization of nitrogen-doped TiO_2 (N–TiO_2) thin films deposited on cylindrical quartz tubes for photocatalytic applications. A binder-free modified dip-coating technique is developed to uniformly immobilize the TiO_2 films, using a sol–gel process with amine-based precursors to control nitrogen doping levels. Thermal annealing ensured strong adhesion of the films to the substrate. Characterization by XRD, UV-vis spectroscopy, FTIR, and XPS confirmed nitrogen incorporation, phase formation, and modifications in band gap and surface chemistry. XPS further detailed the elemental composition and electronic states, highlighting the role of nitrogen in enhancing photocatalytic properties. The visible-light-driven photocatalytic performance is evaluated through the degradation of ciprofloxacin in aqueous medium, with more than 85% degradation efficiency. The improved activity is attributed to effective nitrogen doping and robust film adhesion. This scalable method offers a promising route to producing durable, high-performance photocatalysts for sustainable water treatment technologies.

Received 31st May 2025
Accepted 7th July 2025

DOI: 10.1039/d5ra03856a

rsc.li/rsc-advances

1. Introduction

Transition metal oxide semiconductors are widely recognized as superior photocatalysts for environmental remediation, owing to their optimal light-absorption properties, tunable electronic configurations, and efficient charge-carrier dynamics.[1] Among these, materials such as titanium dioxide (TiO_2), zinc oxide (ZnO), tungsten trioxide (WO_3), tin oxide (SnO_2), and cadmium sulphide (CdS) have demonstrated exceptional efficacy in breaking down diverse organic pollutants through photocatalysis. Notably, TiO_2 has emerged as the most promising candidate in this category, distinguished by its cost-effectiveness, outstanding catalytic activity, good physicochemical stability, robust corrosion resistance, and energy-efficient degradation of pollutants.[2] In comparison, other semiconductor photocatalysts face limitations like (i) instability in aqueous environments, (ii) high rates of electron–hole recombination, and (iii) lower degradation efficiency. The photocatalytic potential of TiO_2 (anatase phase) was first identified by Fujishima in the late 1960s.[3] While TiO_2 demonstrates exceptional photocatalytic properties, it suffers from two critical drawbacks: limited visible-light responsiveness and fast charge carrier recombination. This semiconductor material shows optimal photocatalytic performance mainly under ultraviolet (UV) illumination, which represents merely 4–5% of incident solar radiation. In contrast, visible light makes up around 40% of the solar irradiation spectrum. Therefore, there is a necessity to alter the optical characteristics of TiO_2 to enable it to be active under visible light.

To enhance the visible-light absorption capability of photocatalytic materials, various modification strategies have been developed, controlling crystal formation, tuning particle morphology, functionalizing surfaces, and elemental doping with both metallic and non-metallic species.[4] A highly demanding and efficacious approach to altering the optical characteristics of TiO_2 photocatalysts involves doping with metals (*e.g.*, Mg, Zn, Al, Fe, Cu, *etc.*) and non-metals (N, S, F, P, C).[5] The incorporation of dopant species (either metallic or non-metallic) within the TiO_2 crystal structure can modify the band edge positions and generate new intermediate energy states within the semiconductor's band gap. These introduced states enable electron excitation to the conduction band at lower energy thresholds compared to pristine TiO_2. For effective semiconductor modification, the doping concentration must be optimal; at higher doping concentrations, might function as a recombination centre for charge carriers (electrons and holes) produced through light absorption. Consequently, enhancing the ratio of entrapment to recombination rates while modifying the photocatalyst is critical.[6] Nitrogen is select as a dopant due to its advantageous features such as comparable atomic size to

---

[a] *Department of Chemical Engineering, Indian Institute of Technology Kharagpur, Kharagpur 721302, India. E-mail: rahulbinjhade@gmail.com; smondal@che.iitkgp.ac.in; Fax: +91-3222-255303; Tel: +91-3222-214580*

[b] *Department of Chemical Engineering, Indian Institute of Petroleum & Energy, Visakhapatnam 530003, India. E-mail: rakam.che@iipe.ac.in*

† Electronic supplementary information (ESI) available. See DOI: **https://doi.org/10.1039/d5ra03856a**

oxygen, low ionisation energy, capacity to create metastable centres, and stability, making it more appealing than other anionic elements. Nitrogen-doped TiO_2 is a promising photocatalyst for (continuous-) flow reactors due to its ability to absorb visible light, resulting from a reduced bandgap after nitrogen incorporation. This enables efficient pollutant degradation using sunlight or low-energy visible-light LEDs. In continuous systems, N–TiO_2 is typically immobilized on supports like glass or monoliths, reducing catalyst loss and enhancing stability. Its improved charge separation and surface activity lead to higher degradation and mineralization efficiency, making it ideal for treating pharmaceutical, dye, and pesticide wastewater. Vaiano *et al.*, (2015) synthesized N-doped TiO_2 *via* a sol–gel route using TTIP and ammonia at controlled cryogenic temperatures, with Triton X-100 as a binder dissolved in isopropyl alcohol. The process achieved an optimal crystallite size of 6–17 nm, a 2.5 eV band gap, and an N/Ti molar ratio of 18.6. A four-layer coating on glass spheres, followed by calcination at 450 °C, delivered the best photocatalytic performance.[7] Jagadale *et al.*, (2008) synthesized Undoped TiO_2 *via* a peroxide sol–gel method using TTIP, ethanol, water, and H_2O_2, followed by IR drying and calcination at 300 °C. For N–TiO_2, ethylmethylamine was added as a nitrogen source, yielding nanoparticles (2–14 nm) with a 2.75 eV band gap; nitrogen retention was optimal below 400 °C.[8] Nitrogen-doped TiO_2 was immobilized on glass spheres for ciprofloxacin degradation, with doping levels ranging from 0 to 0.85 wt% by Xing *et al.*, (2018). As nitrogen content increased, the band gap narrowed from 3.2 eV to 2.87 eV, enabling 100% degradation within 3 hours.[9]

Several established methods for narrowing the band gap of TiO_2 through nitrogen doping involve techniques such as sputtering, ion implantation, high-temperature sintering of the photocatalyst, the sol–gel method, oxidation of titanium nitride, and plasma treatment. The sol–gel procedure is often regarded as the most effective and commonly used method for doping due to its simplicity in controlling doping levels and particle sizes. Due to the useful features of the sol–gel method, nitrogen-doped TiO_2 is synthesized using this approach and subsequently employed in the photocatalytic reactors.

Batch reactors generally do not function under steady-state conditions, making them impractical for large-scale industrial use. In continuous processes, catalysts can be employed either as suspended slurry particles or in a fixed immobilized form. However, recovering and reusing catalysts in slurry form can be challenging and expensive due to the additional steps required in the process. Immobilizing the catalyst helps address these issues. Nonetheless, achieving uniformity and smoothness when immobilizing photocatalysts on various supports is difficult. Key concerns include the surface geometry—which can limit scalability—and ensuring proper adhesion of the photocatalyst. Photocatalyst immobilization on various substrates can be achieved through heat treatment or by using a binder.[10] Heat treatment can lead to challenges in achieving a uniform coating. In contrast, binders, such as acrylics, can reduce degradation efficiency by limiting liquid–solid interaction between the photocatalyst layer and the contaminant solution. This reduction occurs because binder molecules occupy active sites, replacing photocatalyst molecules, and hinder light penetration through the binder layer. Consequently, the photocatalytic activity is compromised due to these factors.[10] Although, photocatalysts can be immobilized on substrates of various shapes, the two most fundamental geometries are cylindrical and flat.

Flat surfaces are inherently limited by a low photocatalyst area relative to the floor space, inconsistent light irradiation, and inefficient illumination distribution. To overcome these limitations, immobilizing photocatalysts on cylindrical surfaces is often preferred, as it offers improved illumination and more uniform light distribution. However, achieving a homogeneous photocatalyst coating along the azimuthal direction of a cylindrical tube remains a significant challenge. Immobilizing doped photocatalysts on cylindrical quartz tube without a binder presents a significant challenge in this work. Various methods, such as dip coating or immersion deposition, aerosol spraying, chemical vapour deposition (CVD), and spin coating, can achieve catalyst immobilization.[11] Among these, dip coating is preferred due to its simplicity, cost-effectiveness, and efficiency. In contrast, spray coating often results in non-homogeneous layers, overspray wastage, and poor adhesion. Spin coating is limited to flat surfaces, while CVD is restricted to specific photocatalysts and faces challenges like high cost, complexity, environmental concerns, and slow deposition rates. Although classical dip coating is a cost-effective and widely used method for photocatalyst immobilization on various substrates, it presents challenges when applied to long cylindrical substrates, such as quartz tubes. For instance, coating a large cylindrical substrate (*e.g.*, an 18 mm diameter, 20 cm long tube open at both ends) using conventional dip coating requires a tank slightly exceeding the substrate's length, leading to excessive coating solution consumption. Additionally, selectively coating only the outer surface of such tubes proves particularly difficult with conventional dip coating techniques, further limiting its practicality for such geometries. Coating solutions that predominantly rely on organic solvents pose safety concerns due to the risks of vapour release and flammability. Moreover, maintaining the consistency and quality of the solution in a large tank can be challenging. Each new substrate introduced has the potential to introduce contaminants, which may alter the solution's characteristics. Over time, certain components of the solution may be depleted as more substrates are processed, leading to inconsistencies in the produced thin films. Additionally, solvent evaporation at the surface where substrates are immersed can further impact the solution's composition.[12] Conventional dip coating exhibits limitations for tubular substrates, particularly in solution consumption and exterior deposition. To overcome these constraints, a modified apparatus was developed for efficient exterior photocatalyst immobilization on cylindrical tubes. Optimal parameters were adopted from previous systematic investigations,[13] enabling solution-efficient uniform coatings.

The annular flow shell-and-tube photocatalytic reactor offers superior efficiency and scalability compared to other continuous-flow designs. Unlike monolithic reactors (limited light penetration), microchannel reactors (high cost/complexity), or fluidized beds (catalyst attrition issues), its annular geometry ensures optimal light exposure, low pressure drop, and stable catalyst immobilization. It also outperforms falling-film reactors in flow uniformity and scalability. With balanced performance in mass transfer, irradiation efficiency, and operational simplicity, this design is ideal for industrial-scale photocatalytic applications like water and air purification. Abdulrahman *et al.*, (2022) prepared a 1–5 wt% N–TiO_2 coating solution, applied it to iron sheets *via* spray coating, and achieved 94% degradation of ciprofloxacin in a continuous-flow reactor.[14] Hemanathan *et al.*, (2024) synthesized N–TiO_2 using ammonia as a nitrogen source and used it for naproxen degradation under sunlight, highlighting its solar-driven efficiency in continuous flow system.[15] For gaseous toluene, Sun *et al.*, (2024) used urea, melamine, and ammonium hydroxide as nitrogen sources, varying the N/Ti molar ratio from 1 to 10. Their packed-bed reactor study showed that ammonium hydroxide-derived N–TiO_2 achieved the highest efficiency (96%), demonstrating the importance of precursor selection.[16]

Ciprofloxacin (CIP), a synthetic antibiotic of the fluoroquinolone class, is frequently detected in various water sources due to its widespread use in human and veterinary medicine. It enters aquatic systems primarily through wastewater from drug production facilities, inappropriate medication disposal practices, and biological excretion from living organisms.[17,18] The persistence of ciprofloxacin in the environment raises significant concerns about its impact on both ecological systems and public health. Removing ciprofloxacin from water is critical for several reasons, such as environmental antibiotic exposure promotes the development of drug-resistant bacterial strains, creating serious public health threats, ciprofloxacin can adversely affect aquatic organisms, disrupting microbial communities and harming biodiversity, Contaminated water sources can lead to adverse health effects in humans, including gastrointestinal issues and long-term health risks.[19] Addressing ciprofloxacin contamination is essential for safeguarding water quality, protecting ecosystems, and combating the global challenge of antibiotic resistance.

2. Experimental

2.1 Chemicals and materials

The chemical reagents used in this study are sourced from commercial suppliers: titanium(IV) isopropoxide ($C_{12}H_{28}O_4Ti$, density 0.96 g cm^{-3}) and ciprofloxacin are obtained from Sigma-Aldrich (India), while 30% hydrogen peroxide solution (H_2O_2, density 1.11 g cm^{-3}) was procured from Merck (India). Ethylamine solution 70% (C_2H_7N, density-0.803), diethylamine 99% ($(C_2H_5)_2NH$, density-0.704) and triethylamine 99% ($(C_2H_5)_3N$, desity-0.725) purchased from Loba Chemie, India. The experimental setup utilized quartz tubes (inner diameter: 18 mm, outer diameter: 20 mm, wall thickness: 1 mm, length: 200 mm) sourced from Kedar Scientific Pvt. Ltd (Mumbai, India). All the analysis samples and experimental solutions are prepared using deionized water.

2.2 Synthesis of nitrogen-doped TiO_2 and quartz tube coating procedure

For the synthesis of undoped TiO_2, a solution was prepared by mixing 5 mL of titanium(IV) isopropoxide with 10 mL of absolute ethanol, followed by dilution with 50 mL of deionized water. After mixing for 15 minutes, a white suspension forms, which was then washed 2–3 times with distilled water to eliminate the generated alcohol. After washing, 10 mL of hydrogen peroxide (H_2O_2) was added, resulting in a clear orange peroxide sol. This sol gradually thickens into a gel after about 8 hours. The obtained gel was subjected to thermal treatment, first undergoing drying at 100 °C for solvent evaporation followed by calcination at 400 °C to produce undoped TiO_2 nanoparticles. The present method is an adaption of the previously reported work[8] with modifications, tailored for this application (Fig. 1).

For nitrogen doping, ethylamine, diethylamine, and triethylamine serve as nitrogen sources. Instead of adjusting the N/Ti ratio, a fixed volume of 270 μL of the nitrogen source was used. The nitrogen source was added slowly to the solution, which was stirred continuously for 24 hours to yield a yellowish sol. The synthesized sol underwent sequential thermal treatment, beginning with vacuum drying at 100 °C (12 hour) to remove solvents, followed by programmed calcination at three temperature regimes (400 °C, 450 °C, 500 °C; 2 hour each) to generate thermally differentiated N-doped TiO_2 samples. For immobilization, the yellowish sol was coated onto the exterior surface of quartz cylindrical tubes, after which it undergoes a drying and calcination process with same temperatures as maintained for power samples.

For coatings involving doped or undoped TiO_2 and other photocatalysts, the expense of the coating solution can become considerable, particularly when dealing with large substrates, such as a cylindrical tube measuring 20 cm in length with a 20 mm outer diameter. Conventional dip coating techniques require substantial volumes of solution. To mitigate this, a modified dip coating system was designed, that coats the

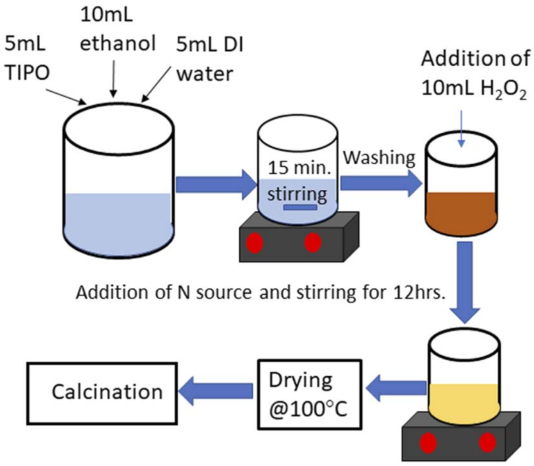

Fig. 1 Schematic representation of the sol–gel synthesis process for nitrogen-doped TiO_2 powder preparation and thin film coating procedure.

exterior surface of quartz cylindrical tubes while utilizing only a small amount of solution (10–15 mL). The coating process involves the deposition of nitrogen-doped TiO_2 onto quartz tubes using customized dip-coating equipment. The synthesized coating solution exhibits a viscosity around 3995 mPa s. A single layer was applied while maintaining a constant motor speed of 400 rpm. The coating duration was 30 minutes, followed by subsequent drying and calcination processes to ensure proper film formation. All description and design of dip coater equipment was reported in our previous article.[13] The optimal conditions for achieving high degradation efficiency and strong adhesion are found to be three layers of coating process applied to exterior of quartz tubes while rotating it at 400 rpm.

2.3 Photocatalytic reaction

A shell-and-tube continuous flow photocatalytic reactor was employed for the effective elimination of ciprofloxacin (1 mg L^{-1} concentration) from aqueous waste streams. The solvent used to prepare the ciprofloxacin solution was deionized water. Two steel connectors with diameters lower than the outer casing were used to fit a quartz tube (ID-18 mm, OD-20 mm, and L-200 mm) within the reactor's steel-made outer shell, which has ID-23 mm and L-220 mm. There was a 20 mL-volume annular space between the outer casing and steel-mad quartz tube where the working solution flow. For the photodegradation reaction, a 12W visible LED (violet light, 400 ± 10 nm wavelength) strip was inserted within a quartz tube. In the drug degradation experiments, two reactors of the same configuration in series were used. For scenarios involving extended residence durations and minimal flow velocities, a series configuration of three to four interconnected reactors presents a viable solution.

Fig. 2 illustrates the reactor configuration incorporating a 50 mL syringe infusion pump connected through a tubing network, with vertical fluid delivery from the upper to lower reactor ports. Since it was a continuous operation, flow rate of 4.5 mL per hour was maintained by syringe pump. The experiment lasts 8 hours, 1 hour of dark reaction was carried out and then in each 2-hour interval we collect 1 mL of sample. The collected sample was analysed by LCMS-MS to determine the concentration change over time. Liquid chromatography was carried out using XTerra MS C-18 (3 µm, 2.1 mm × 100 mm) column coupled with a photodiode array detector, employing an isocratic mobile phase consisting of deionized water and acetonitrile (70 : 30 v/v) delivered at 0.25 mL min^{-1} flow rate.

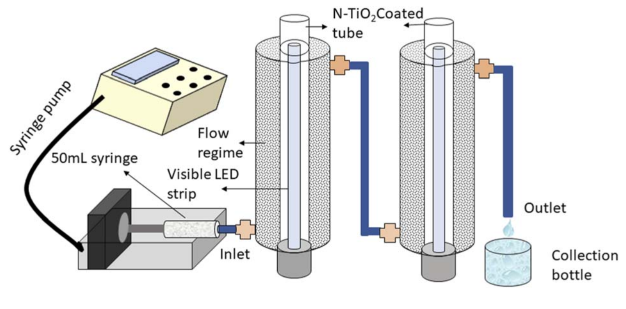

Fig. 2 Schematic of the photocatalytic degradation system for ciprofloxacin (1 ppm) treatment employing a 12-watt visible light LED array as the illumination source.

For pharmaceutical degradation studies, a dual-reactor series configuration was employed. Under conditions requiring extended hydraulic retention times and reduced flow velocities, expanding the system to three or four sequentially connected reactors offers an effective operational solution.

All experiments are repeated thrice, and the mean value of the measurements are reported.

3. Analysis

3.1 UV-visible spectrophotometric analysis

Absorbance measurements are conducted using a SHIMADZU 2600I UV-Vis-NIR spectrophotometer, with spectral data recorded across the 200–800 nm wavelength range to generate characteristic absorption profiles.

3.2 Crystallographic characterization

The X-ray diffraction plots was recorded using the PANalytical X'Pert3 Powder system, employing K-Alpha1 radiation with a wavelength of 1.540598 Å and K-Alpha2 radiation with a wavelength of 1.544426 Å. The scan was conducted over a 2θ angle range of 10° to 80° at a scanning speed of 0.04 s^{-1}.

3.3 Fourier transform infrared (FTIR) spectroscopic characterization

Fourier-transform infrared spectra of the N-doped TiO_2 samples are acquired using a PerkinElmer Spectrum 100 spectrometer with universal ATR attachment, employing potassium bromide pellet preparation for transmission measurements.

3.4 Field emission scanning electron microscopy (FESEM)

Surface morphology and coating uniformity are characterized using a JEOL JSM-7610F field emission scanning electron microscope, investigating the effects of deposition parameters including: (i) coating layer multiplicity, (ii) substrate rotation velocity, and (iii) precursor solution viscosity on film microstructure.

3.5 X-ray photoelectron spectroscopy (XPS)

The nitrogen percentage in sol–gel-prepared nitrogen-doped TiO_2 samples was analysed using a Physical Electronics instrument (Model: PHI5000 VersaProbe III). This equipment was also employed to investigate the elemental states (Ti, N, C, and O) present in the sample. The analysis was performed in survey scan mode with a pass energy of 280 eV, utilizing K-alpha aluminium radiation as the source, which has a photon energy of 1486.6 eV.

3.6 Liquid chromatography mass spectroscopy (LC-MS/MS) quantitative analysis

Ciprofloxacin concentration profiles are monitored using a Waters 2695 LC system coupled to a QuattroMicro™ API tandem mass spectrometer (Waters Corp., USA). Chromatographic separation was achieved on an XTerra MS C-18 column (2.1 × 100 mm, 3 μm) with isocratic elution using an acetonitrile-water mobile phase (30 : 70, v/v) at 0.25 mL min^{-1} flow rate. Detection parameters included: UV monitoring at 200–400 nm and 10 μL injection volumes for optimal analyte resolution.

3.7 Rheological characterization of the coating solution

The viscosity of the photocatalyst coating solution was measured using an Anton Paar MCR 102e rheometer with a cone-plate geometry configuration, maintaining a fixed gap distance of 105 μm between the measuring surfaces.

3.8 Optical surface profilometer analysis

The surface roughness (thickness) of nitrogen-doped TiO_2 photocatalyst coated on a cylindrical tube was measured using an Anton Paar Micro Combi Tester (Model: OPX). The profilometer operates in a contactless mode, and a microscope with 5× magnification was used to select the region of analysis.

4. Result and discussion

4.1 Ultraviolet-visible spectroscopy (UV-vis DRS)

UV-visible diffuse reflectance spectroscopy was utilized to evaluate the light absorption characteristics and band gap energies of both pure and nitrogen-doped TiO_2 samples. Due to the technical challenges associated with measuring coated films on cylindrical substrates, powdered N-doped TiO_2 photocatalysts are prepared *via* the previously described sol–gel method for optical analysis. The coating process employed the as-synthesized sol without binders, followed by thermal treatment. Fig. 3a and b present comparative absorbance spectra (200–800 nm range) of commercial TiO_2 and synthesized N–TiO_2, with the visible light region commencing at 400 nm.

The optical bandgap energies of both doped and undoped TiO_2 photocatalysts are determined using the widely adopted Tauc plot method, as referenced in prior literature.[20]

$$\alpha h\nu = \alpha_0(h\nu - E_g)^n \quad (1)$$

Physical significant of each term present in the Tauc plot was already discussed in our previous work.[13] The optical absorption analysis reveals a substantial increase in visible-range photon absorption (400–800 nm) for N-doped TiO_2 relative to undoped commercial TiO_2. Among the synthesized nitrogen-doped samples, EA + NH_3-400 shows the highest absorbance capacity within the 400 to 800 nm range (visible light spectrum), outperforming the others in visible light absorption. Further increasing the amine concentration did not significantly alter the band gap energy of the nitrogen-doped photocatalyst, as evidenced by the negligible changes observed in Fig. S1 (ESI section).† Additionally, the higher amine content adversely affected the coating solution properties, leading to poor adhesion of the photocatalyst onto the outer surface of the quartz tube. This compromised immobilization likely resulted from altered viscosity or colloidal stability, preventing uniform deposition during the coating process.

To further reduce the band gap energy, we employed a combination of ammonia and amine as nitrogen sources. The precursor volumes were kept consistent, with 270 μL of amine and 20 mL of ammonia solution used in each case. Doping was performed under these conditions for three different amines: ethylamine (EA), diethylamine (DEA), and triethylamine (TEA). Interestingly, all three cases yielded nearly identical band gap values of approximately 2.8 eV, which was consistent with previsous literature report.[8,9] Given this consistency, only the EA + NH_3-400 sample was included in the UV-vis absorbance graph for comparative analysis.

The increase in band gap observed at higher calcination temperatures may be attributed to the thermal desorption or evaporation of nitrogen from the TiO_2 lattice. Alternatively, the amine precursors used for nitrogen doping may decompose at elevated temperatures, losing their ability to retain nitrogen within the TiO_2 structure. This leads to a reduction in nitrogen incorporation, thereby increasing the band gap due to decreased doping efficiency. A violet light (LED) with an emission range of 400–450 nm was intentionally chosen as the

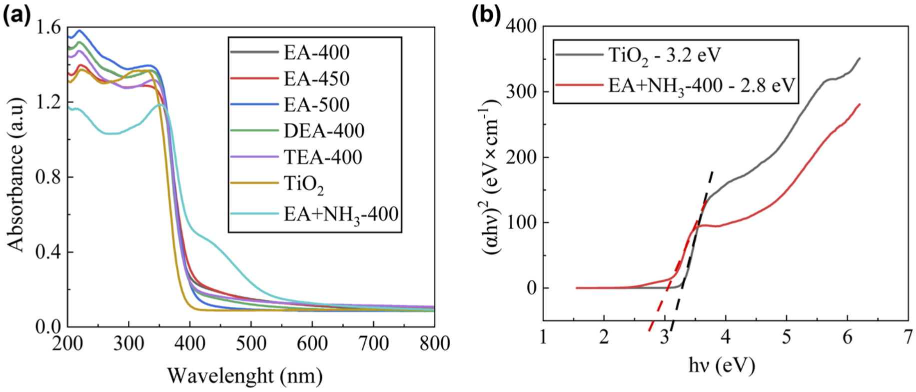

Fig. 3 (a) UV-vis absorption spectra comparing commercial TiO_2 and N–TiO_2 photocatalyst powders, showing enhanced visible-light absorption (400–800 nm) for the doped sample relative to the undoped material. (b) Tauc plot analysis comparing the optical bandgap energies of commercial TiO_2 and N–TiO_2 powders, derived from UV-vis absorption data.

Table 1 Details of the synthesis conditions for all nitrogen-doped TiO_2 powder and coated samples

Sample name	Description
EA400	TiO_2 doped with nitrogen using ethylamine as source of nitrogen. Volume of ethylamine added was 270 μL and calcination temperature is 400 °C
EA450	TiO_2 doped with nitrogen using ethylamine as source of nitrogen. Volume of ethylamine added was 270 μL and calcination temperature is 450 °C
EA500	TiO_2 doped with nitrogen using ethylamine as source of nitrogen. Volume of ethylamine added was 270 μL and calcination temperature is 500 °C
DEA400	TiO_2 doped with nitrogen using diethylamine as source of nitrogen. Volume of diethylamine added was 270 μL and calcination temperature is 400 °C
TEA400	TiO_2 doped with nitrogen using triethylamine as source of nitrogen. Volume of triethylamine added was 270 μL and calcination temperature is 400 °C
EA + NH_3-400	TiO_2 doped with nitrogen using ethylamine and ammonia as source of nitrogen. Volume of nitrogen sources added are ethylamine 270 μL and 20 mL of ammonia solution and calcination temperature was 400 °C
TiO_2	TiO_2 synthesised using the same sol–gel method

Table 2 Band gap energy of nitrogen doped TiO_2 samples, synthesized at various conditions as per the description in Table 1

Sample name	Band gap energy (eV)	N (%)
EA-400	3.06	2.33
EA-450	2.91	1.37
EA-500	3.16	1.35
EA + NH_3-400	2.81	2.75
DEA-400	3.09	0.77
TEA-400	3.11	0.58
TiO_2	3.26	—

irradiation source for photocatalytic degradation experiments. This selection was based on the UV-vis spectra results (Fig. 3a), which revealed a significant redshift in the absorption edge of the optimally nitrogen-doped TiO_2 sample, specifically within the 400–500 nm range. Since this sample exhibited the strongest visible-light response in this region, the violet LED ensures efficient activation of the photocatalyst, maximizing degradation efficiency under visible-light irradiation. Table 2 summarizes the optical bandgap values determined for all fabricated TiO_2-based materials.

4.2 XRD analysis

The XRD pattern was recorded using a PANalytical X'Pert3 Powder system, utilizing K-alpha1 radiation with a wavelength of 1.540598 Å and K-alpha2 radiation at 1.544426 Å. The measurements are taken over a 2θ range of 10 to 70°, with a scan speed of 0.04 s^{-1}.

Fig. 4 displays the XRD diffraction patterns for both doped and undoped TiO_2. According to JCPDS CARD 00-021-1272,[21] the peak positions along the 2θ axis correspond to the anatase phase, appearing at 25.2, 37.6, 44.5, 47.7, 53.7, 54.8, and 62.32°, with the primary anatase peak located at 25.2. The diffraction peaks of nitrogen-doped TiO_2 exhibit distinct variations in both profile morphology (shape) and relative intensity when compared to undoped TiO_2. The reduced intensity in N–TiO_2's diffraction pattern provide direct evidence of successful nitrogen integration into the Titania crystal structure.[8,22] The introduction of nitrogen into the TiO_2 structure reduces the crystallinity of the material, leading to noticeable variations in peak height between the doped and undoped TiO_2 in the XRD patterns.[23] Upon nitrogen doping, N atoms substitute oxygen sites or occupy interstitial positions within the TiO_2 lattice. This incorporation introduces localized lattice distortions and modifies the electron density distributions, which reduces the X-ray scattering efficiency and consequently decreased peak intensities. Notably, if the doping was homogeneous and induces minimal strain or defects, peak broadening may remain negligible while intensity diminishes. The observed reduction in peak intensity (particularly at ~25°) arises from two primary effects: (1) a slight disruption in long-range crystallinity due to N incorporation, and (2) the lower atomic scattering factor of N compared to O, which attenuates constructive X-ray interference.

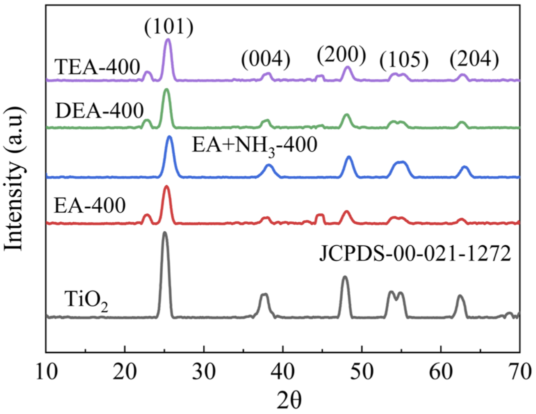

Fig. 4 XRD patterns of commercial TiO_2 and N–TiO_2 samples synthesized using different nitrogen precursors, with all doped materials calcined at 400 °C.

4.3 FTIR analysis

Fig. 5 presents the FTIR spectra of commercial TiO_2 alongside various nitrogen-doped TiO_2 powder prepared using amine-based nitrogen sources. The infrared vibrations are nearly identical across all samples. The low wavenumber bands, ranging from 500 to 800 cm^{-1}, are associated with Ti–O–Ti vibrations.[22] The FTIR spectrum reveals a weak absorption band at 1380 cm^{-1}, characteristic of N–O vibrational stretching modes, confirming successful nitrogen doping through the formation of N–O bonds within the TiO_2 crystal structure. The presence of these vibrations suggests nitrogen doping, which can occur either by substitution or interstitially within the lattice structure. A weak peak at 2345 cm^{-1} corresponds to N–H

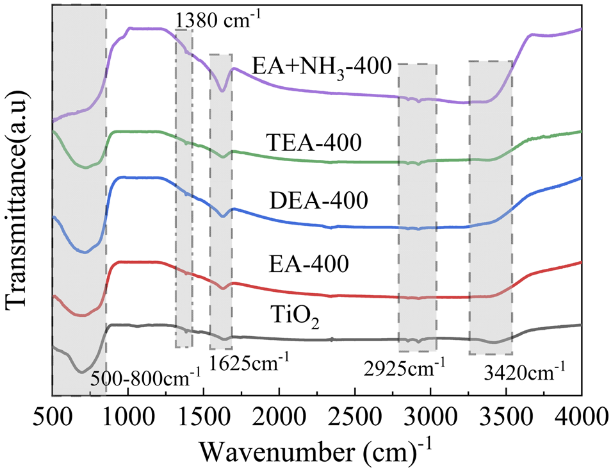

Fig. 5 Comparative FT-IR spectra of TiO_2 and nitrogen-doped TiO_2 samples prepared with different nitrogen precursors, showing characteristic vibrational modes associated with surface modifications.

stretching, confirming nitrogen incorporation when ethylamine (EA), diethylamine (DEA) triethylamine (TEA) are used as doping agents. The absorption band at 2925 cm^{-1} arises from C–H stretching vibrations, confirming residual organic compounds.[23,24] Peaks observed at 3420 cm^{-1} and 1625 cm^{-1} correspond to Ti–OH symmetric stretching and O–H bending modes, respectively, associated with surface hydroxyl groups and adsorbed water molecules. Comparative analysis reveals markedly enhanced peak intensities in N-doped TiO_2 relative to undoped TiO_2,[9,25] demonstrating that nitrogen incorporation promotes surface hydroxylation and water adsorption – critical factors for improved photocatalytic performance. Complementary evidence of nitrogen doping was provided by XPS characterization.

4.4 XPS analysis

XPS analyses the binding energies of electrons emitted from a material's surface, with each element having specific binding energies related to its core electrons. In the case of nitrogen-doped TiO_2, shifts in the binding energies of Ti, O, and N suggest alterations in their chemical states resulting from nitrogen incorporation. Fig. 6a represents a comparative analysis of the XPS full survey spectra for pure TiO_2 and the EA + NH_3-400 sample. Both spectra exhibit characteristic peaks corresponding to Ti, O, and C at identical binding energy positions, confirming the preservation of the primary electronic structure following nitrogen doping. Notably, the EA + NH_3-400 sample displays a weak but distinct nitrogen peak around 400 eV, indicating successful incorporation of N species into the TiO_2 matrix.

Nitrogen can incorporate into the TiO_2 lattice in two primary ways: substitutional and interstitial nitrogen. In substitutional nitrogen, a Ti–O–Ti bond was replaced by a Ti–O–N bond, while interstitial nitrogen involves the formation of NO or NO_2 species. The presence of a single peak around 400 eV indicates that NO or NO_2 formation was not occurring. Instead, nitrogen atoms easily substitute oxygen atoms within the Ti–O–Ti framework.[8,9,22,23] Fig. 6b highlights the nitrogen peak at a binding energy of 400 eV across all N-doped TiO_2 samples. Fig. 7 shows that the peak with the highest intensity, at 528.5 eV, corresponds to the oxygen 1s state. The XPS analysis consistently detected characteristic peaks between 528 and 529 eV binding energy in all examined samples, suggesting uniform surface chemical states. Oxygen at 528.5 eV was identified as crystal lattice oxygen (OL), which primarily arises from Ti–O bonds within the TiO_2 crystal lattice. N-doped TiO_2 exhibits characteristic Ti 2p doublet peaks at 457 eV (Ti $2p_{3/2}$) and 463 eV (Ti $2p_{1/2}$), demonstrating clear spin–orbit splitting as shown in Fig. 8. These values are associated with the presence of Ti^{4+} ions. The consistent Ti 2p peaks across all samples, regardless of nitrogen precursor concentration, suggest that the amount of nitrogen precursor used has minimal impact on the

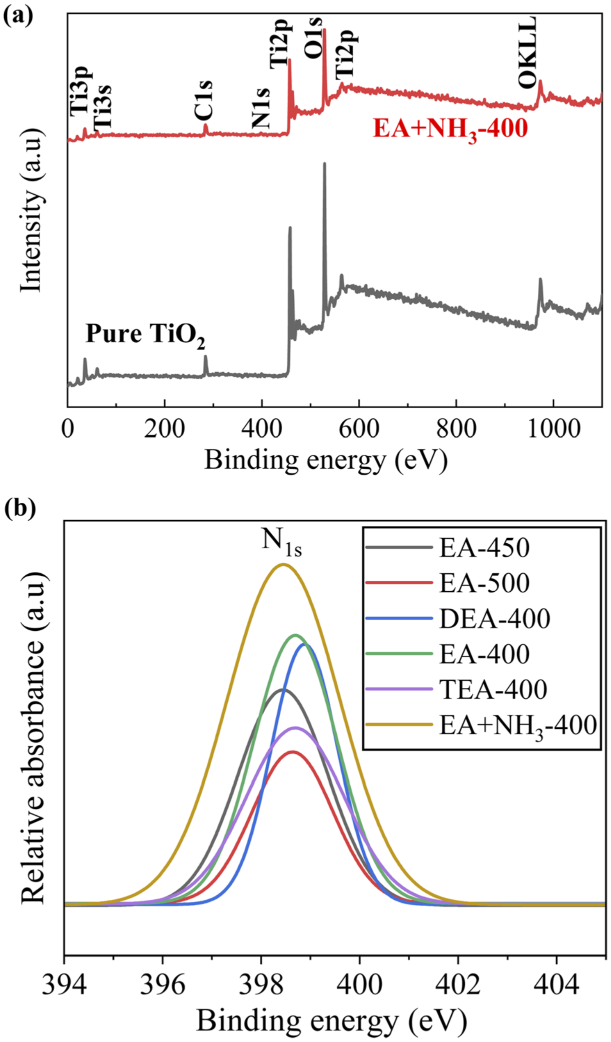

Fig. 6 (a) XPS full survey spectra of pure and nitrogen-doped TiO_2 samples, showing characteristic binding energy peaks corresponding to different elements chemical states. (b) XPS spectra of the N 1s region for nitrogen-doped TiO_2 samples, showing characteristic binding energy peaks corresponding to different nitrogen chemical states.

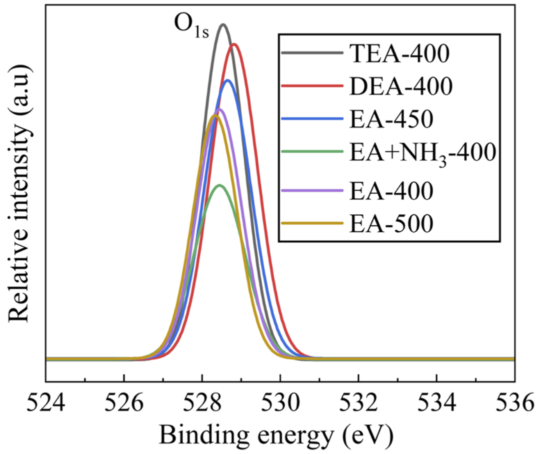

Fig. 7 O 1s XPS spectra of nitrogen-doped TiO_2 samples, showing characteristic binding energy peaks corresponding to different oxygen chemical environments.

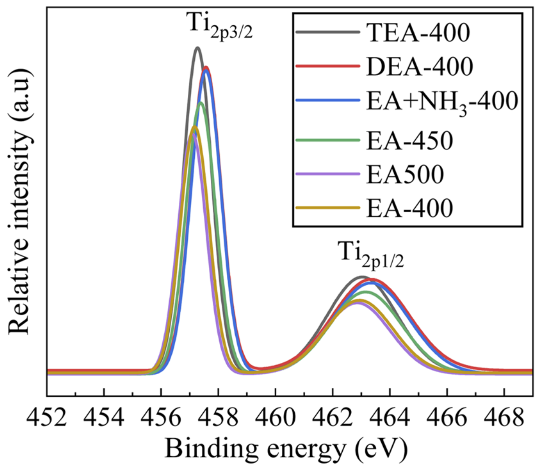

Fig. 8 Ti2p XPS spectra of nitrogen-doped TiO_2 samples, showing spin–orbit split doublet peaks ($2p_{3/2}$ and $2p_{1/2}$) characteristic of titanium oxidation states.

electronic structure of nitrogen-doped TiO_2.[26,27] This study employed XPS characterization to quantitatively analyse nitrogen content (atomic %) across all synthesized N–TiO_2 photocatalysts, with results tabulated in Table 2.

4.5 Scanning electron microscopy (SEM) imaging

We have used Field Emission-SEM (FESEM) imaging to analyse the coating features, and the tendency of the solid particles to form agglomerates within the coated films. The samples are coated with gold (∼2–3 nm) to improve the surface conductivity for enhanced resolution and clarity in imaging. The SEM images provide insights into the microstructural features of films prepared using a modified dip-coating technique (recorded at magnification 500 00X).

FESEM examination confirmed the successful deposition of a uniform nitrogen-doped TiO_2 layer on the quartz tube's exterior surface through the enhanced dip-coating approach, as evidenced in Fig. 9. Multiple regions of the coating are examined through FESEM, and the images appeared consistent across all analysed areas of the tube.

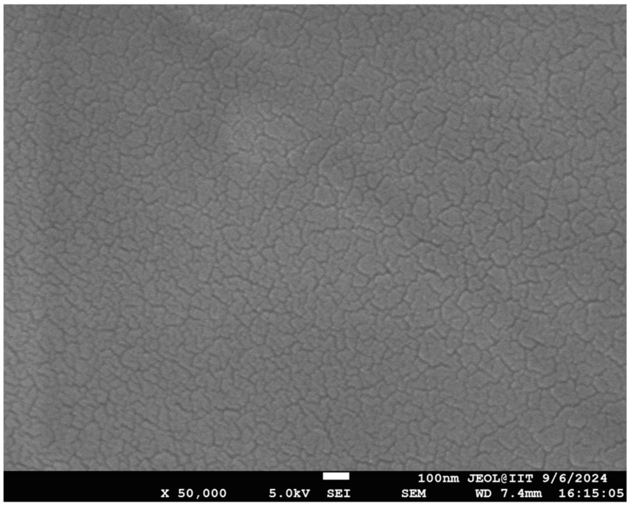

Fig. 9 FESEM micrographs of N-doped TiO_2 coatings on quartz tube substrates shown at 50 000× magnification, demonstrating the nanoscale surface topography and coating uniformity.

4.6 Coating solution rheology analysis

Fig. 10 illustrates the rheological profile of the surface treatment (coating) solution as-synthesized *via* the sol–gel method. The results indicate that the solution exhibits Newtonian fluid behaviour. The viscosity of the solution has an impact in achieving a uniform and homogeneous coating layer. If the solution was too viscous, it may result in a thick, non-uniform coating. This non-homogeneity can be attributed to the leaching of N–TiO_2 from the coating surface after calcination. On the other hand, a solution with very low viscosity can lead to an

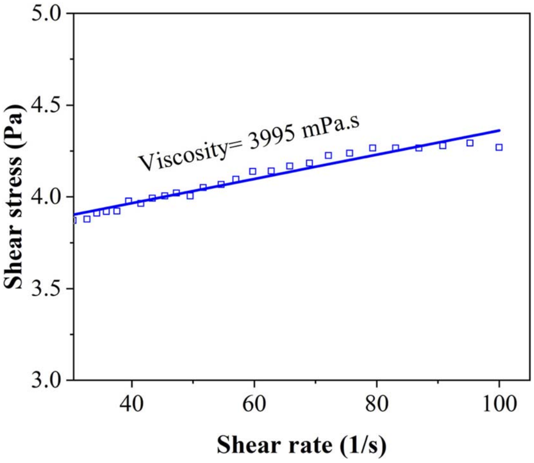

Fig. 10 Rheological analysis of sol–gel prepared nitrogen-doped TiO_2 coating solution, behaviour assessment and viscosity calculation. The experimental data is shown in symbols and the solid line represent the linear fit, to estimate the viscosity.

excessively thin coating, which contains insufficient catalyst for effective drug degradation experiments. Therefore, achieving an optimal viscosity was essential for ensuring the quality and performance of the coating layer.

4.7 Surface profilometer analysis

Table 3 summarizes the measured thickness and surface roughness characteristics of the photocatalyst films deposited on cylindrical substrates. The surface topography was quantitatively assessed using two key parameters: R_a (arithmetic average roughness) and R_q (root mean square roughness), with reduced values corresponding to enhanced surface smoothness. According to Table 3, the (mean) thickness of the coated (surface treated) photocatalyst layer over the quartz tube was measured to be 14 μm (difference of the R_a values between the coating and uncoated samples). Kannangara *et al.*, (2018) evaluated the roughness of nitrogen-doped TiO_2 thin films on glass substrates. Their results showed that the film thickness varied between 4.9 and 30.2 μm, highlighting the variation in surface profile depending on coating conditions and deposition methods. This supports the relevance of surface roughness measurements in thin film characterization.[28] The R_q parameter suggests the variance to the mean roughness (R_a), and values up to 100 μm are considered good for coating applications.

4.8 Photocatalytic degradation

The photocatalytic breakdown mechanism initiates with CIP molecule adsorption *via* its functional groups, followed by aromatic ring cleavage and progressive transformation into simpler intermediates, consistent with established aqueous-phase organic pollutant degradation pathways.[13]

LC-MS/MS was employed to characterize transformation products generated during the visible-light-driven (violet light 405 nm) photocatalytic breakdown of ciprofloxacin using N–TiO_2 as the active photocatalyst.

Fig. 11 outlines the stepwise photocatalytic degradation mechanism, where oxidative attack predominantly occurs at the piperazine C–N bond *via* direct hole oxidation. This initial cleavage forms dialdehyde intermediate P1 (*m*/*z* 362), which undergoes sequential transformations: (i) piperazine ring opening and decarboxylation to P2 (*m*/*z* 334),[29] (ii) secondary decarboxylation yielding P3 (*m*/*z* 306), (iii) methylamide elimination producing P4 (*m*/*z* 291),[30] and (iv) subsequent carbonyl loss and decarboxylation generating P5 (*m*/*z* 263) and P6 (*m*/*z* 219).[31,32] Terminal defluorination completes the mineralization pathway, forming P7 (*m*/*z* 200).

Table 3 Surface roughness analysis of photocatalyst coatings under varying deposition conditions [values in parentheses indicate coating-specific roughness parameters (R_a, R_q)]

Roughness parameters	Blank (without coating) sample	Coated sample
R_a (μm)	39.5	53.5
R_q (μm)	84.6	98.9

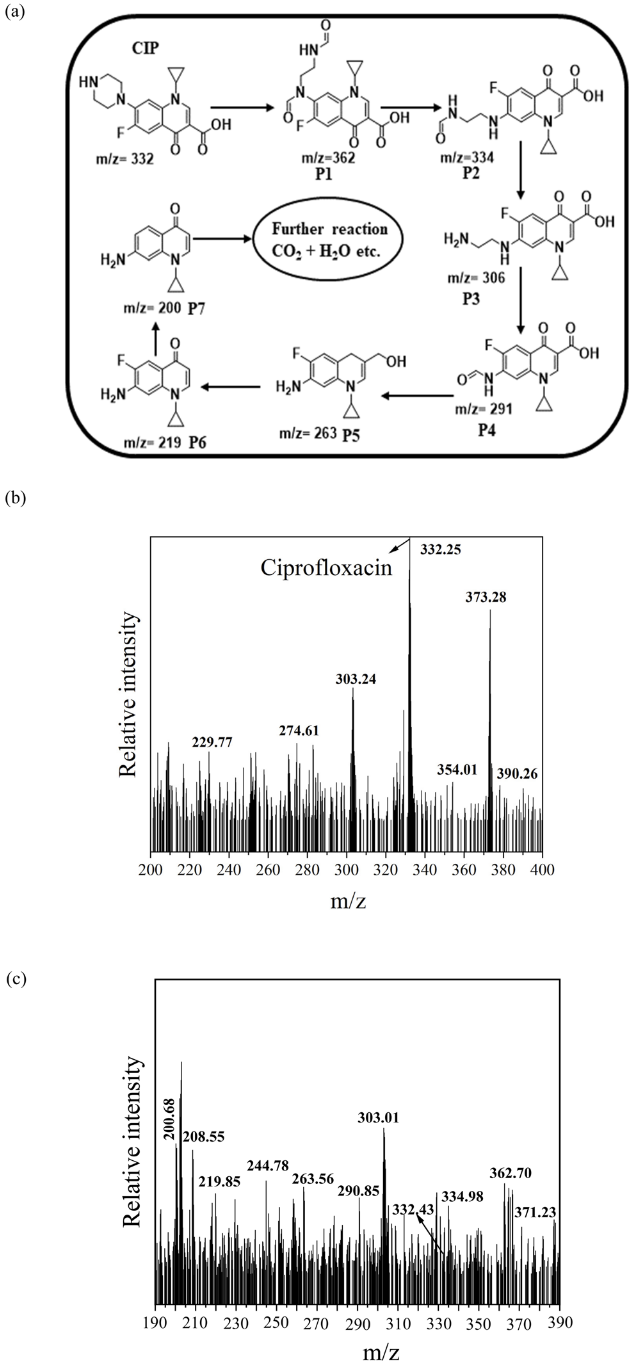

Fig. 11 (a) Schematic of the continuous-flow photocatalytic degradation system for ciprofloxacin, featuring N-doped TiO_2-coated tubular reactor, 12W visible LED array illumination source and sequential pollutant transformation mechanism. MS spectrum of the (b) CIP, and the (c) reaction intermediates obtained at the end of 9 hours of experiment.

Ciprofloxacin was photo-catalytically degraded in a continuous-flow annular reactor immobilized with N–TiO_2 as the active photocatalyst. The experiments are conducted till the (pseudo-) steady state, which was somewhat beyond the residence time (around 8 hours) of the system. The outlet stream (treated effluent) was not mixed or recycled with the feed. This

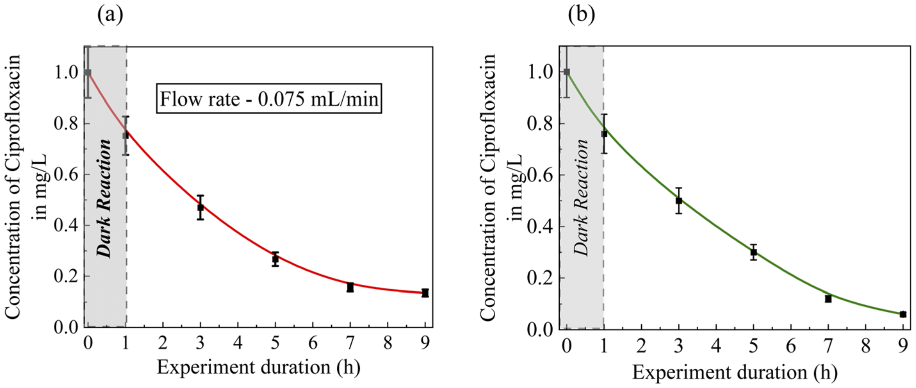

Fig. 12 (a) Continuous-flow and (b) batch photocatalytic degradation of ciprofloxacin (CIP), in an annular reactor system employing N–TiO_2-coated quartz tubes. The errors bars represent the uncertainty of the experimental measurements. The solid line shows the trend behaviour.

study examines how effectively the TiO_2-coated tube removes the drug and evaluates the level of degradation efficiency that can be achieved for ciprofloxacin. The nitrogen-modified TiO_2 photocatalyst activity efficiency was analysed by the pollutant degradation measurement. Fig. 12 shows the time-dependent degradation of CIP when using an immobilized photocatalyst on a cylindrical tube, prepared under specific processing conditions. All reactor trials employed continuous operation with precisely controlled hydrodynamic conditions (0.075 mL min^{-1} flow rate, τ = 8.5-hour residence time) to ensure optimal contact duration. The immobilized photocatalyst film was photo-activated using a 405 nm wavelength LED light source (12W power output) in the visible spectrum. As illustrated in Fig. 12, approximately 25% of CIP degradation was attributed to adsorption on the active sites of the photocatalyst immobilized on the tube's outer surface, with an overall degradation efficiency (from adsorption and visible light exposure) reaching around 86% after 9 hours of experiment. Comparable results have been reported in previous investigations on the photocatalytic degradation of other pharmaceutical drugs in continuous-flow systems, where degradation efficiencies typically ranged between 80% and 90%.[9,33] Abdulrahman *et al.* (2022) reported 89% removal efficiency under continuous-flow conditions.[14] Similarly, Lima *et al.* (2014) and Binjhade *et al.* (2025) achieved 85% and 92% degradation efficiencies, respectively, using continuous-flow photocatalytic reactor setups.[34,35]

A comparative study of CIP photocatalytic degradation was conducted under batch and continuous flow modes using a shell-and-tube (annular) photocatalytic reactor. Identical experimental conditions were maintained in both systems, except for the absence of any flow in the batch operation mode. During the initial dark reaction phase (first hour), approximately 24–25% CIP degradation was observed in both the case, attributed primarily to adsorption onto the catalyst surface. After 9 hours of irradiation, the degradation efficiency reached 94% in batch mode, compared to 86% in continuous flow operation (see Fig. 12). The marginally higher efficiency in the batch system may be linked to prolonged contact time between the pollutant and catalyst, enhancing photocatalytic activity.

4.9 Photocatalyst reuse study

To evaluate the reusability and stability of the photocatalyst, two coated quartz tubes were employed in a continuous-flow photocatalytic reactor for CIP degradation. Following each 9-hour reaction cycle, the tubes were thoroughly rinsed with deionized water and reused for subsequent experiments. This process was repeated for five consecutive cycles to assess the long-term performance of the catalyst. The results demonstrated excellent adhesion and stability of the N–TiO_2 coating, with only a minimal decrease in photocatalytic efficiency over multiple uses. During the first three cycles, the CIP degradation efficiency remained consistently high at approximately 86%. Even after five cycles, the degradation efficiency only slightly declined to 83%, representing a negligible reduction of just 3% (see Fig. 13). These findings confirm that the immobilized N–TiO_2 catalyst exhibits strong reusability with minimal loss of activity, making it a promising candidate for sustainable wastewater treatment applications.

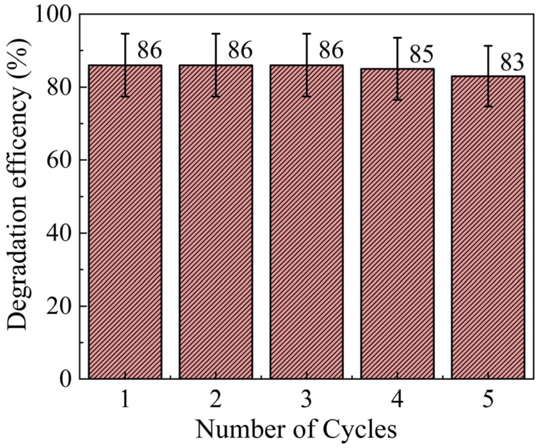

Fig. 13 Catalyst reuse study for photocatalytic degradation of ciprofloxacin (CIP) in a continuous flow annular reactor system employing N–TiO_2-coated quartz tubes. The errors bars represent the uncertainty of the experimental measurements. The solid line shows the trend behaviour.

Nitrogen-doped TiO_2 (N–TiO_2) has demonstrated effective photocatalytic activity under visible light for the degradation of various pharmaceutical compounds in continuous-flow systems. Several classes of pharmaceutical pollutants—including antibiotics (*e.g.*, ciprofloxacin, tetracycline), non-steroidal anti-inflammatory drugs (NSAIDs) like ibuprofen and diclofenac, beta-blockers such as atenolol and metoprolol, and anticonvulsants like carbamazepine.—have been successfully degraded using N–TiO_2 in continuous photocatalytic reactors. The degradation efficiencies vary depending on operating conditions, but typically range from 70% up to 90%.

5. Conclusion

This study successfully synthesized nitrogen-doped TiO_2 through a sol–gel method, with the EA + NH_3-400 sample exhibiting the most favourable properties for visible-light photocatalysis. UV-vis absorption spectroscopy and Tauc plot analysis confirmed a reduced bandgap of 2.8 eV for EA + NH_3-400, significantly lower than that of undoped TiO_2 and other modified samples, indicating enhanced visible-light absorption. XRD analysis verified nitrogen incorporation into the TiO_2 lattice, as evidenced by peak broadening and intensity variations, while FTIR spectroscopy further supported doping through the presence of characteristic N-related absorption bands at 1620 cm^{-1} and 3410 cm^{-1}. XPS results confirmed successful nitrogen doping, with the EA + NH_3-400 sample displaying the highest nitrogen content (2.85%) and a distinct N1s peak at 400 eV. Photocatalytic degradation experiments demonstrated that EA + NH_3-400 effectively removes 86% of ciprofloxacin (CIP) under visible LED irradiation (12W), highlighting its potential for wastewater treatment applications. Notably, the catalyst maintained excellent stability over five reuse cycles with minimal efficiency loss (<5% degradation drop), underscoring its practical potential.

The findings of this work contribute to the development of efficient visible-light-active photocatalysts for environmental remediation. Future studies should explore (1) the long-term stability and reusability of nitrogen-doped TiO_2 under continuous operation, (2) the optimization of doping concentrations to further enhance photocatalytic efficiency, and (3) the applicability of this material for degrading other emerging pharmaceutical pollutants under real-world conditions. Additionally, mechanistic studies using advanced techniques such as transient absorption spectroscopy could provide deeper insights into charge carrier dynamics and further improve photocatalytic performance.

Data availability

The data reported in this work are available in the ESI.†

Conflicts of interest

There are no conflicts to declare.

References

1 R. Ahmad and R. Kumar, Adsorption studies of hazardous malachite green onto treated ginger waste, *J. Environ. Manage.*, 2010, **91**(4), 1032–1038.
2 V. K. Gupta, A. Rastogi, V. K. Saini, *et al.*, Biosorption of copper(II) from aqueous solutions by *Spirogyra* species, *J. Colloid Interface Sci.*, 2006, **296**(1), 59–63.
3 C. M. Ling, A. R. Mohamed and S. Bhatia, Performance of photocatalytic reactors using immobilized TiO_2 film for the degradation of phenol and methylene blue dye present in water stream, *Chemosphere*, 2004, **57**(7), 547–554.
4 R. Marschall and L. Wang, Non-metal doping of transition metal oxides for visible-light photocatalysis, *Catal. Today*, 2014, **225**, 111–135.
5 R. Bendoni, E. Mercadelli, N. Sangiorgi, *et al.*, Alternative route for the preparation of Zr-doped TiO_2 layers for energy and environmental applications, *Ceram. Int.*, 2015, **41**(8), 9899–9909.
6 R. Singh and S. Dutta, A review on H2 production through photocatalytic reactions using TiO_2/TiO_2-assisted catalysts, *Fuel*, 2018, **220**, 607–620.
7 V. Vaiano, O. Sacco, D. Sannino and P. Ciambelli, Nanostructured N-doped TiO_2 coated on glass spheres for the photocatalytic removal of organic dyes under UV or visible light irradiation, *Appl. Catal., B*, 2015, **170**, 153–161.
8 T. C. Jagadale, S. P. Takale, R. S. Sonawane, *et al.*, N-doped TiO_2 nanoparticle based visible light photocatalyst by modified peroxide sol–gel method, *J. Phys. Chem. C*, 2008, **112**(37), 14595–14602.
9 X. Xing, Z. Du, J. Zhuang and D. Wang, Removal of ciprofloxacin from water by nitrogen doped TiO_2 immobilized on glass spheres: rapid screening of degradation products, *J. Photochem. Photobiol., A*, 2018, **359**, 23–32.
10 J. Kumar and A. Bansal, A comparative study of immobilization techniques for photocatalytic degradation of Rhodamine B using nanoparticles of titanium dioxide, *Water, Air, Soil Pollut.*, 2013, **224**, 1–11.
11 R. Binjhade, R. Mondal and S. Mondal, Continuous photocatalytic reactor: critical review on the design and performance, *J. Environ. Chem. Eng.*, 2022, **10**(3), 107746.
12 B. L. Brophy, S. Maghsoodi and P. J. Neyman, Coating and Curing Apparatus and Methods, *US Pat.*, 8960123, 2015.
13 R. Binjhade, R. Mondal and S. Mondal, Photocatalyst immobilisation on cylindrical surface: scale-up potential of continuous photocatalytic reactor, *Mater. Chem. Phys.*, 2024, **328**, 130018.
14 S. A. Abdulrahman, Z. Y. Shnain, S. S. Ibrahim and H. S. Majdi, Photocatalytic degradation of ciprofloxacin by UV light using N-doped TiO_2 in suspension and coated forms, *Catalysts*, 2022, **12**(12), 1663.
15 G. Hemanathan, S. Karthikeyan and R. Kathirvel, Comparative study on solar photocatalytic degradation of naproxen using nitrogen doped ZnO and nitrogen doped

TiO_2: kinetics and intermediates analysis, *Desalin. Water Treat.*, 2024, **320**, 100675.

16 Y. Sun, Y. Ahmadi and K.-H. Kim, The selection of a nitrogen precursor for the construction of N-doped titanium dioxide with enhanced photocatalytic activity for the removal of gaseous toluene, *Environ. Res.*, 2024, **260**, 119664.

17 T. Paul, M. C. Dodd and T. J. Strathmann, Photolytic and photocatalytic decomposition of aqueous ciprofloxacin: transformation products and residual antibacterial activity, *Water Res.*, 2010, **44**, 3121–3132.

18 M. Yoosefian, S. Ahmadzadeh, M. Aghasi, *et al.*, Optimization of electrocoagulation process for efficient removal of ciprofloxacin antibiotic using iron electrode; kinetic and isotherm studies of adsorption, *J. Mol. Liq.*, 2017, **225**, 544–553.

19 M. Malakootian, A. Nasiri and M. A. Gharaghani, Photocatalytic degradation of ciprofloxacin antibiotic by TiO_2 nanoparticles immobilized on a glass plate, *Chem. Eng. Commun.*, 2020, **207**(1), 56–72.

20 H. Lin, C. P. Huang, W. Li, *et al.*, Size dependency of nanocrystalline TiO_2 on its optical property and photocatalytic reactivity exemplified by 2-chlorophenol, *Appl. Catal., B*, 2006, **68**(1–2), 1–11.

21 M. Mollavali, C. Falamaki and S. Rohani, Preparation of multiple-doped TiO_2 nanotube arrays with nitrogen, carbon and nickel with enhanced visible light photoelectrochemical activity *via* single-step anodization, *Int. J. Hydrogen Energy*, 2015, **40**(36), 12239–12252.

22 X. Cheng, X. Yu and Z. Xing, Characterization and mechanism analysis of N doped TiO_2 with visible light response and its enhanced visible activity, *Appl. Surf. Sci.*, 2012, **258**(7), 3244–3248.

23 X. Cheng, X. Yu, Z. Xing and L. Yang, Synthesis and characterization of N-doped TiO_2 and its enhanced visible-light photocatalytic activity, *Arabian J. Chem.*, 2016, **9**, S1706–S1711.

24 P. Praveen, G. Viruthagiri, S. Mugundan, *et al.*, Structural, optical and morphological analyses of pristine titanium dioxide nanoparticles—Synthesized *via* sol–gel route, *Spectrochim. Acta, Part A*, 2014, **117**, 622–629.

25 J. Yang, H. Bai, X. Tan, *et al.*, IR and XPS investigation of visible-light photocatalysis—Nitrogen–carbon-doped TiO_2 film, *Appl. Surf. Sci.*, 2006, **253**(4), 1988–1994.

26 J. Du, G. Zhao, Y. Shi, *et al.*, A facile method for synthesis of N-doped TiO_2 nanooctahedra, nanoparticles, and nanospheres and enhanced photocatalytic activity, *Appl. Surf. Sci.*, 2013, **273**, 278–286.

27 Y. H. Lin, C. H. Weng, A. L. Srivastav, *et al.*, Facile synthesis and characterization of N-doped TiO_2 photocatalyst and its visible-light activity for photo-oxidation of ethylene, *J. Nanomater.*, 2015, **2015**(1), 807394.

28 Y. Y. Kannangara, R. Wijesena, R. M. G. Rajapakse and K. M. N. de Silva, Heterogeneous photocatalytic degradation of toluene in static environment employing thin films of nitrogen-doped nano-titanium dioxide, *Int. Nano Lett.*, 2018, **8**(1), 31–39.

29 A. Salma, S. Thoröe-Boveleth, T. C. Schmidt, *et al.*, Dependence of transformation product formation on pH during photolytic and photocatalytic degradation of ciprofloxacin, *J. Hazard. Mater.*, 2016, **313**, 49–59.

30 H. Liang, M. Yu, J. Guo, *et al.*, A novel vacancy-strengthened Z-scheme g-C3N4/Bp/MoS2 composite for super-efficient visible-light photocatalytic degradation of ciprofloxacin, *Sep. Purif. Technol.*, 2021, **272**, 118891.

31 K. Hu, R. Li, C. Ye, *et al.*, Facile synthesis of Z-scheme composite of TiO_2 nanorod/g-C3N4 nanosheet efficient for photocatalytic degradation of ciprofloxacin, *J. Cleaner Prod.*, 2020, **253**, 120055.

32 Z. Jia, T. Li, Z. Zheng, *et al.*, The BiOCl/diatomite composites for rapid photocatalytic degradation of ciprofloxacin: efficiency, toxicity evaluation, mechanisms and pathways, *Chem. Eng. J.*, 2020, **380**, 122422.

33 R. K. S. Mhemid, M. S. Salman and N. A. Mohammed, Comparing the efficiency of N-doped TiO_2 and commercial TiO_2 as photo catalysts for amoxicillin and ciprofloxacin photo-degradation under solar irradiation, *J. Environ. Sci. Health, Part A*, 2022, **57**(9), 813–829.

34 M. J. Lima, M. E. Leblebici, M. M. Dias, J. C. B. Lopes, C. G. Silva, A. M. T. Silva and J. L. Faria, Continuous flow photo-Fenton treatment of ciprofloxacin in aqueous solutions using homogeneous and magnetically recoverable catalysts, *Environ. Sci. Pollut. Res.*, 2014, **21**, 11116–11125.

35 R. Binjhade, R. Mondal and S. Mondal, Photocatalytic degradation of ciprofloxacin and metformin in a continuous-flow tubular reactor, *React. Chem. Eng.*, 2025, **10**, 1577–1586.